



THE UNIVERSITY *of* EDINBURGH

Edinburgh Research Explorer

High-Pressure Structural Systematics in Samarium to 222 GPa

Citation for published version:

Finnegan, S, Pace, E, Storm, C, McMahon, M, MacLeod, SG, Liermann, H & Glazyrin, K 2020, 'High-Pressure Structural Systematics in Samarium to 222 GPa', *Physical Review B*, vol. 101, no. 17, 174109. <https://doi.org/10.1103/PhysRevB.101.174109>

Digital Object Identifier (DOI):

[10.1103/PhysRevB.101.174109](https://doi.org/10.1103/PhysRevB.101.174109)

Link:

[Link to publication record in Edinburgh Research Explorer](#)

Document Version:

Peer reviewed version

Published In:

Physical Review B

General rights

Copyright for the publications made accessible via the Edinburgh Research Explorer is retained by the author(s) and / or other copyright owners and it is a condition of accessing these publications that users recognise and abide by the legal requirements associated with these rights.

Take down policy

The University of Edinburgh has made every reasonable effort to ensure that Edinburgh Research Explorer content complies with UK legislation. If you believe that the public display of this file breaches copyright please contact openaccess@ed.ac.uk providing details, and we will remove access to the work immediately and investigate your claim.



New High-Pressure Structural Systematics in Samarium to 222 GPa

S. E. Finnegan, E. J. Pace, C. V. Storm, and M. I. McMahon*
*SUPA, School of Physics and Astronomy, and Centre for Science at Extreme Conditions,
 The University of Edinburgh, Mayfield Road, Edinburgh, EH9 3JZ, UK.*

S. G. MacLeod
*AWE, Aldermaston, Reading RG7 4PR, United Kingdom and
 SUPA, School of Physics and Astronomy, and Centre for Science at Extreme Conditions,
 The University of Edinburgh, Mayfield Road, Edinburgh, EH9 3JZ, UK.*

H.-P. Liermann and K. Glazyrin
*Deutsches Elektronen-Synchrotron (DESY), Notkestrasse 85, D-22607 Hamburg, Germany
 (Dated: April 9, 2020)*

Angle-dispersive x-ray powder diffraction experiments have been performed on samarium metal up to 222 GPa. Up to 50 GPa we observe the Sm-type ($hR9$) \rightarrow dhcp ($hP4$) \rightarrow fcc ($cF4$) \rightarrow distorted-fcc ($hR24$) \rightarrow $hP3$ transition sequence reported previously. The structure of the high-pressure phase above 93 GPa, previously reported as having a monoclinic structure with space group $C2/m$, is found to be orthorhombic, space group $Fddd$, with 8 atoms per unit cell ($oF8$ in Pearson notation). This structure is the same as that found in Am, Cm and Cf at high pressures. Analysis of samarium’s equation of state reveals marked changes in compressibility in the $hP3$ and $oF8$ phases, with the compressibility of the $oF8$ phase being that of a “regular” metal.

PACS numbers:

I. INTRODUCTION

The lanthanide series of elements is characterized by the monotonic filling of the $4f$ electron shell and the members of the series play an important role in many modern technologies, including high-performance permanent magnets, catalysts, and computer memories. As one traverses the series, the predominantly trivalent lanthanide elements (La to Lu, excluding Ce, Eu and Yb) exhibit a reduction in their atomic radii, the well-known lanthanide contraction, and a change in the ambient-conditions crystal structure that correlates with changes in the d -band occupancy¹. The same structural sequence – hcp \rightarrow Sm-type \rightarrow dhcp \rightarrow fcc \rightarrow distorted-fcc (dfcc) ($hP2 \rightarrow hR9 \rightarrow hP4 \rightarrow cF4 \rightarrow hR24$ in Pearson notation) – can be induced via compression in individual lanthanide elements as a result of increased occupation of the $5d$ states arising from pressure-induced s -to- d electron transfer^{2,3}. The structures of all these phases comprise different stacking of close-packed or quasi-close-packed layers, and Raman scattering studies on Sm to 20 GPa⁴ have reported that the structural sequence involves softening of optical and acoustic modes implying also anomalies in the elastic behaviour of the different phases. There are no measurable volume changes between the phases, but further compression of the $hR24$ phase results in first-order phase transitions to the so-called “collapsed” phases, the lower-symmetry structures of which have long been reported to arise from the participation of $4f$ electrons in the bonding⁵, although more recent studies have questioned this⁶⁻⁹.

In Nd and Sm, the initial post- $hR24$ phase is reported to be rhombohedral with spacegroup $P3_121$ and 3 atoms

per unit cell ($hP3$ in Pearson notation) and is obtained via a small volume change of $\sim 0.4\%$ ¹⁰. On further compression, these two elements are then reported¹¹ to transform into a monoclinic structure (spacegroup $C2/m$, $mC4$ in Pearson notation) first observed in Ce at high pressure over 40 years ago¹². The same $mC4$ structure is reported in the collapsed phases of Gd, Tb, Dy, Ho, Er and Tm, all of which are obtained via a direct first-order transition from the $hR24$ phase rather than via the intermediate $hP3$ phase¹³⁻¹⁷.

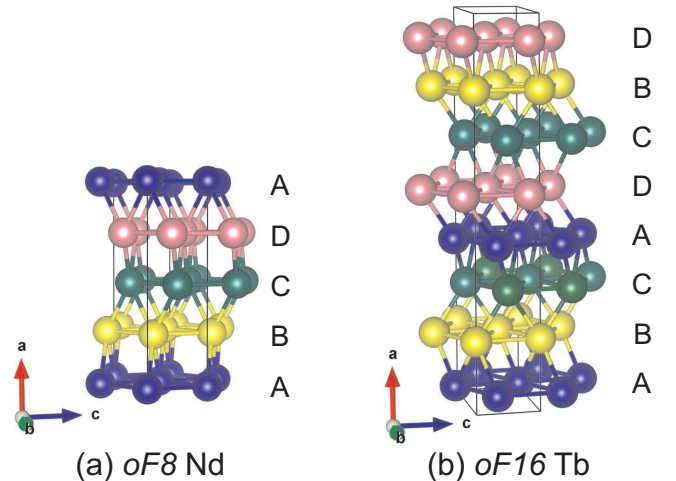


FIG. 1: The crystal structures of (a) $oF8$ -Nd at 89 GPa and (b) $oF16$ -Tb at 64 GPa. The structures are iso-symmetric with the $Fddd$ space group, and differ in the stacking of their flat, hcp-like atomic layers: the stacking sequence in $oF8$ is ABCD while in $oF16$ it is ABCADCBD.

We have recently shown that the long-reported $mC4$ structure is incorrect in Tb, and also in Gd, Dy, Ho, Er and Tm, and that the true structure of these collapsed phases is orthorhombic, space group $Fddd$, with 16 atoms per unit cell (hereafter $oF16$)¹⁸. While isosymmetric with the 8-atom $Fddd$ structure found in Am, Cm and Cf at high pressures^{19–21}, the $oF16$ structure comprises an 8-layer ABCADCBD stacking of quasi-hcp layers, as opposed to the 4-layer ABCD repeat seen in $oF8$ - see Figure 1. However, the nature of the stacking in the two structures is the same, with the atoms in each layer centred above the midpoint of two atoms in the previous layer, resulting in both having 10-fold (6+2+2) coordination. We have also reported that the $hP3$ structure of Sm actually has spacegroup $P6_222$ rather than $P3_121$, and that it has the same stacking as the $oF8$ and $oF16$ structures, although with a 3-layer ABC stacking sequence¹⁸. Finally, we have noted that the reported diffraction profiles from the $mC4$ phase of Nd²² are remarkably similar to those from the $oF8$ phase of Am, Cm and Cf, and that the published d -spacings of Nd at 89 GPa²² can be fitted perfectly with this orthorhombic structure¹⁸. The collapsed $oF8$, $oF16$ and $hP3$ phases are thus all members of the same family of quasi-close-packed layer structures, differing only in the stacking sequence of the layers. The same structures are also seen in both the lanthanide and actinide elements.

The single trivalent lanthanide element whose high-pressure behaviour does not seem to follow the same structural sequence is Sm¹¹. While the post- $hP3$ phase is reported to have the same $mC4$ structure initially found in Nd²², the reported diffraction patterns from Sm are dissimilar to those obtained from any other collapsed phase¹¹, including Nd, suggesting it has neither the $oF16$ nor the $oF8$ structure. To investigate whether Sm does indeed have a different sequence of high-pressure phases to any other lanthanide element, we have performed x-ray powder diffraction studies of Sm to 222 GPa. We find that the post- $hP3$ phase does indeed have the same $oF8$ structure seen in Nd, Am, Cm and Cf and that this phase is stable to at least 222 GPa. We suggest that the diffraction pattern reported previously as coming from the $mC4$ phase was, in fact, from a mixed-phase sample of $hP3$ and $oF8$.

II. EXPERIMENTAL DETAILS

High-purity distilled samples of Sm supplied by Ulrich Schwarz at the Max-Planck-Institut für Chemische Physik fester Stoffe in Dresden were loaded into three diamond-anvil cells (DACs) in a dry argon atmosphere (<1 ppm O₂ and <1 ppm H₂O) to prevent oxidation. The DACs were equipped with beveled diamonds with 100 μm culets and tungsten (W) gaskets. The samples were loaded without any pressure medium but with a small copper (Cu) sphere to act as a pressure calibrant, using the recently-published Cu equation of state

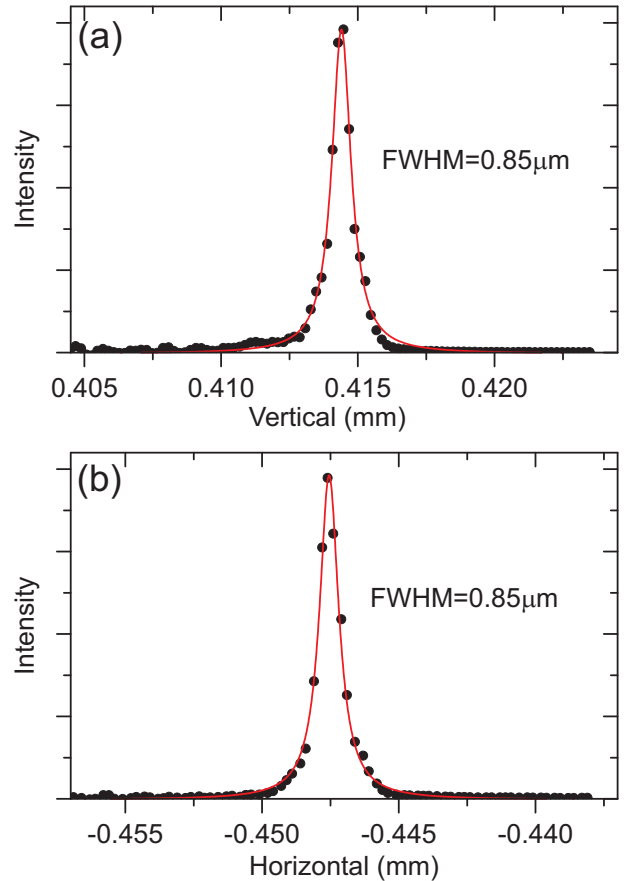


FIG. 2: Scans across the microfocused x-ray beam on the P02.2 beamline, both (a) vertically and (b) horizontally. The exact beamsizes in each direction varies from experiment to experiment, but is typically $0.85 \times 0.85 \mu\text{m}^2$ FWHM, as shown by the two Lorentzian curves.

of Sokolova *et al.*²³.

Diffraction data were collected in two experiments on the Extreme Conditions P02.2 beamline at the PETRA-III synchrotron in Hamburg, and in a third experiment on the high-pressure I15 beamline at the Diamond Light Source (DLS) in the United Kingdom. Monochromatic x-ray beams of wavelength 0.2895Å and 0.4808Å (PETRA-III) and 0.4248Å (DLS), focused down to 3 $\mu\text{m} \times 6 \mu\text{m}$ and 0.85 $\mu\text{m} \times 0.85 \mu\text{m}$ (PETRA-III) and 20 $\mu\text{m} \times 20 \mu\text{m}$ (DLS) were used, and the powder-diffraction data were recorded on Perkin-Elmer (PETRA-III) and Mar345 (DLS) area detectors, placed 300-400 mm from the sample. CeO₂ and LaB₆ diffraction standards were used to calibrate the exact sample-detector distances and the detector tilts. The 2D diffraction patterns collected at each pressure were integrated azimuthally using Fit2D²⁴ and Dioptas²⁵ to obtain standard 1D diffraction profiles, which were then analysed using Rietveld and Le Bail methods or by fitting to the d -spacings of individual diffraction peaks.

The sub-micron diameter beam on the Extreme Con-

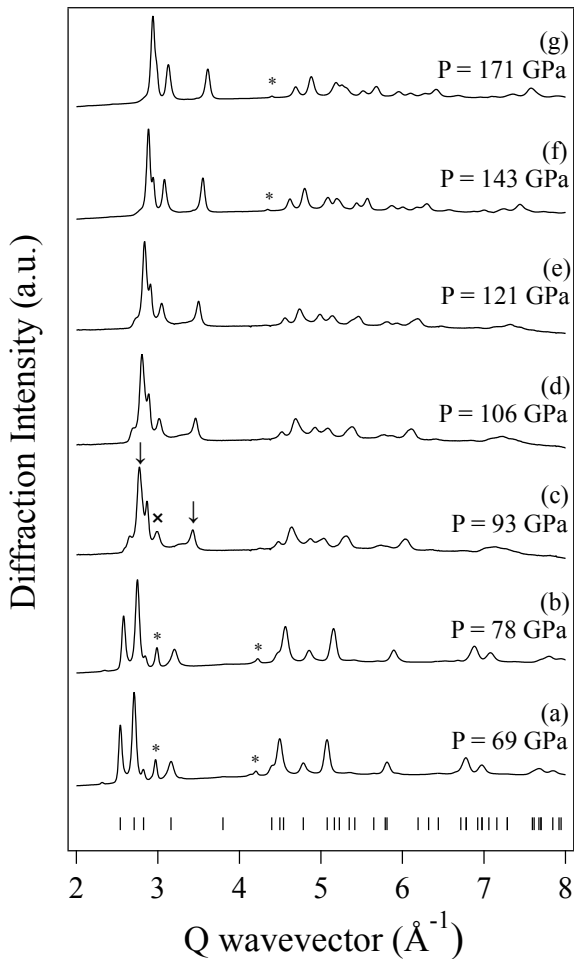


FIG. 3: Diffraction profiles collected from Sm on pressure increase. The data were collected from the same sample during two different synchrotron visits, and so are plotted as a function of wavevector (Q) in order to take account of the two different x-ray wavelengths used. Tick marks beneath profile (a) mark calculated peak positions from the $hP3$ phase. The peaks marked with asterisks are from the W gasket. The arrows in profile (c) marks the first appearance of peaks from the new phase. The reflections labelled with a ‘ \times ’ in profile (c) indicate a doublet including the (101) peak from the W gasket and a peak from the post $hP3$ phase. A single phase pattern of the post $hP3$ phase is seen in profile (g).

ditions P02.2 beamline is a recent development ideally suited to high-pressure diffraction experiments above 200 GPa. The small beam minimizes parasitic scattering from the high- Z metallic gasket surrounding the sample, minimizes pressure gradients in the diffracting sample volume, and also enables calibrant-free diffraction patterns to be obtained from the sample if required. Focusing is achieved by first cutting down the x-ray beam size ~ 35 m from the source to approximately 0.05×0.05 mm² before using 136 Be compound refractive lenses

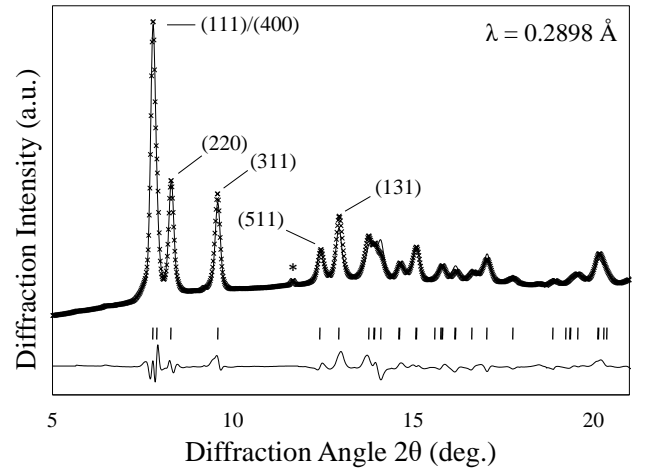


FIG. 4: Rietveld refinement of the $oF8$ structure to a diffraction profile from Sm at 175 GPa, showing the observed (crosses) and calculated (line) diffraction patterns, the calculated reflection positions, and the difference profile ($R_P=2.1\%$, $R_{wP}=3.1\%$, $R_E=2.8\%$, $GoF=1.09$, and $R(F^2)=7.2\%$). The first six peaks of the $oF8$ phase are labelled with their Miller indices, and the asterisk identifies the (200) peak from the W gasket (the (110) peak from the gasket is overlapped by the (220) reflection from the Sm).

(CRLs)²⁶, optimized for use at a fixed x-ray wavelength of 25.6 keV (~ 0.48 Å), to focus only the coherent part of the beam to 0.85×0.85 μm^2 (FWHM) over a focal length of 360 mm (Figure 2). Finally, the focused beam is passed through a 15 μm diameter pinhole immediately before the DAC in order to trim its tails. We have found that a 15 μm pinhole provides the optimum trade off between x-ray flux and the intensity of the parasitic scattering from the W gasket

III. DISCUSSION

Diffraction patterns were first collected from the $hP3$ phase below 50 GPa to ensure consistent results with those collected previously by Husband *et al.*²⁷. The transition to the $hP3$ phase was observed at 42(5) GPa, in excellent agreement with previous studies²⁷. Analysis of the $hP3$ patterns confirmed that the systematic absences were consistent with spacegroup $P6_222$ rather than $P3_121$.

On further compression above 50 GPa (see Figure 3), first evidence of the post- $hP3$ phase was observed at 93(4) GPa (Figure 3, profile (c)). The peaks from the post- $hP3$ phase increased in intensity on further compression (Figure 3, profiles (d)-(f)), and single-phase profiles were obtained above 157 GPa (Figure 3, profile (g)). No further changes were observed up to 222(2) GPa, the highest pressure reached in this study.

The single-phase diffraction profiles obtained above

157 GPa are remarkably similar to those obtained from the *oF8* phase of Nd²². Figure 4 shows a Rietveld fit of the *oF8* structure to the diffraction profile from Sm at 175(2) GPa, where the refined lattice parameters are $a = 8.4250(9)$ Å, $b = 4.5531(3)$ Å, and $c = 2.5227(2)$ Å, $V/V_0=0.364(2)$, with atoms on the $8a$ site at (0,0,0). The fit is excellent, with all of the observed diffraction peaks being indexed.

The *oF8* structure of Sm and Nd, and the *oF16* structure of Tb (see Figure 1), both comprise stackings of flat, quasi-close-packed layers, the distortion of which from hexagonal symmetry can be quantified by the deviation of the b/c ratio from the ideal ortho-hexagonal value of $\sqrt{3}=1.732$. The pressure dependence of the b/c ratio in *oF8*-Sm is shown in Figure 5, along with the ideal value of $\sqrt{3}$ in the *hP3* phase. There is a clear discontinuity in the ‘hexagonality’ of the atomic layers from 1.732 to ~ 1.78 at the *hP3* \rightarrow *oF8* transition, after which the distortion grows slowly and monotonically to reach a maximum value of 1.818(5) at 222 GPa. Our fit to the Nd diffraction pattern reported by Akella *et al.* at 89 GPa revealed a ratio of 1.7847(1) at that pressure¹⁸, the same as that observed in *oF8*-Sm at ~ 132 GPa.

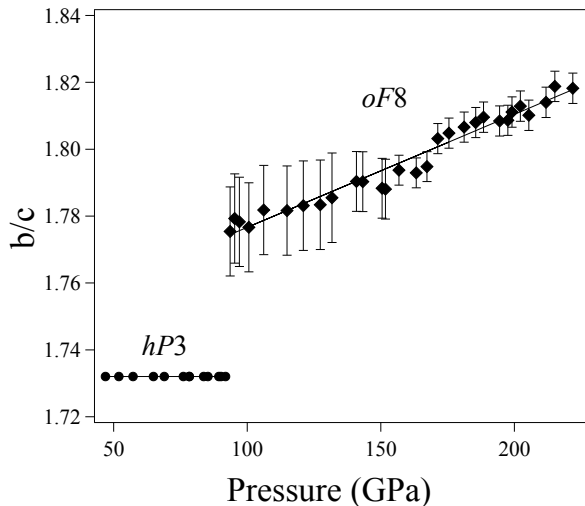


FIG. 5: The pressure dependence of the hexagonality of the atomic layers in the *oF8* phase of Sm. The distortion can be quantified by the deviation of the b/c ratio from the ideal ortho-hexagonal value of $\sqrt{3}$ (1.732). The atomic layers in the *hP3* phase have perfect hexagonal symmetry, and hence have the ideal ortho-hexagonal value. The discontinuity in the geometry of the layers at the *hP3* \rightarrow *oF8* transition at 93 GPa is very clear and suggests that the transition is not continuous.

The similarity of the *oF8*-Sm diffraction patterns reported here with those published previously from *oF8*-Nd above 75 GPa²² raises the question as to why the reported *mC4* structures from the two phases were previously very different^{11,22}. However, it is clear that the diffraction pattern reported from Sm at 109 GPa¹¹ is

not from a single-phase sample of *oF8*-Sm. Comparison of the 109 GPa diffraction pattern reported by Chesnut with the mixed *hP3*-*oF8* profile obtained in the current study at 106 GPa (see Figure 3 profile (d)) reveals them to be very similar. A two-phase *hP3*-*oF8* Le Bail fit to this profile is shown in Figure 6, which reveals that all of the observable peaks are explained by the two-phase model. We therefore suspect that Chesnut’s analysis at 109 GPa was hampered by the use of a profile from a mixed-phase sample. Unfortunately, while that study attained pressures of 200 GPa, where single-phase patterns from the *oF8* phase might be expected, no diffraction profiles were shown above 109 GPa.

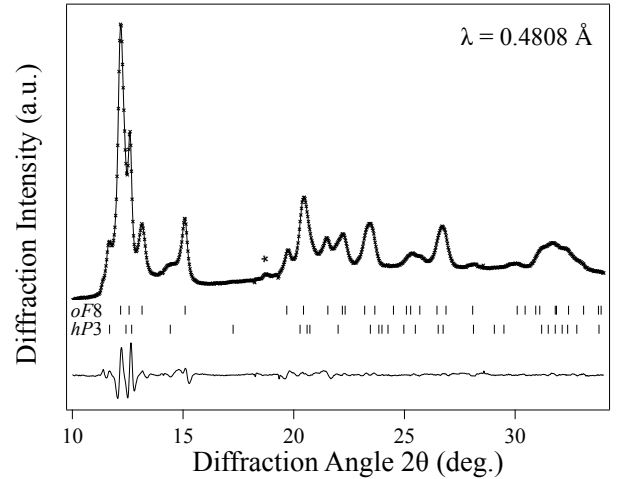


FIG. 6: Le Bail fit of the *hP3* and *oF8* structures to a mixed-phase diffraction profile from Sm at 106 GPa, showing the observed (crosses) and calculated (line) diffraction patterns, the calculated peak positions of the two phases, and the difference profile. The asterisk identifies the (200) peak from the W gasket. This is the same profile as that shown in Figure 3(d).

The compressibility of Sm to 222 GPa, including the data of Husband *et al.* below 50 GPa²⁷, is shown in Figure 7. The similarities of the *hP3* and *oF8* structures, which differ only in the stacking sequence of their hcp-like layers¹⁸, results in a sizable pressure range (for example, 93-157 GPa in one of our samples - see Figure 3) over which mixed *hP3*-*oF8* profiles are observed, and in extensive peak-overlap in this mixed-phase region. The $P6_222$ and $Fddd$ space groups are not group-subgroup related and so the transition between the *hP3* and *oF8* structures need not be second order. Indeed, the sharp discontinuity observed in the geometry of the atomic layers at the *hP3* \rightarrow *oF8* transition (Figure 5) suggests that the transition is not continuous. However, careful analysis of mixed-phase profiles reveals that there is no measurable volume change at the transition, despite the discontinuity in the shape of the atomic layers.

Fits to the compression data of Sm up to 43 GPa (that is, up to the *hR24* \rightarrow *hP3* transition) were made with the

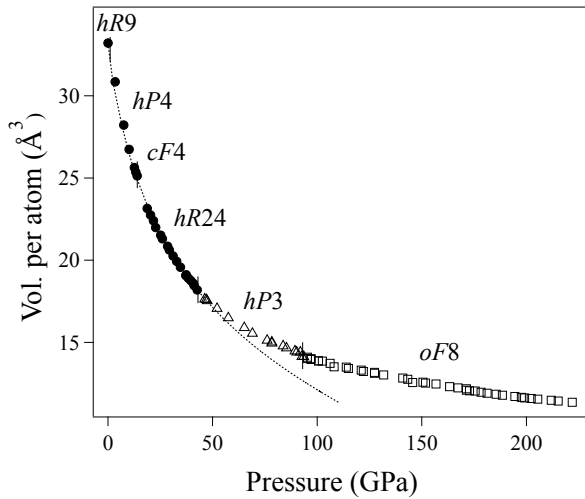


FIG. 7: The compressibility of Sm up to 222 GPa. The dotted line shows the AP2 equation of state obtained from fitting the data to 43 GPa. The misfit beyond 43 GPa can be clearly observed.

second order (AP2) form of the Adapted Polynomial of order L (APL) equation of state (EoS)²⁸

$$P = 3K_0 \frac{(1-x)}{x^5} \exp(c_0(1-x)) \left(1 + x \sum_{k=2}^L c_k (1-x)^{k-1}\right) \quad (1)$$

with K_0 is the zero pressure bulk modulus, K' is its pressure derivative, $x = (V/V_0)^{1/3}$, $c_0 = -\ln(3K_0/p_{FG})$, $c_2 = (3/2) \cdot (K' - 3) - c_0$, $p_{FG} = a_{FG}(Z/V_0)^{5/3}$ is the Fermi-gas pressure, Z is the atomic number, and $a_{FG} = (3\pi^2)/5 \cdot \hbar^2/m_e = 0.02337 \text{ GPa} \cdot \text{nm}^5$ is a constant. This gave an excellent fit with $K_0 = 33.4(5) \text{ GPa}$ and $K' = 3.08(3)$ ²⁹ (see Figure 7). However, extrapolation of this EoS to higher pressures revealed an increasingly poor fit, with the compressibilities of both the $hP3$ and $oF8$ phases above 43 GPa being considerably smaller than that predicted from the extrapolation of the AP2 EoS obtained from the data below that pressure (see Figure 7).

Fits to the full compression curve to 222 GPa using a single AP2 EoS were poor, and the inability of 2nd order EoSs to fit the Sm compression curve has been noted previously by both Zhao³⁰ and Chesnut¹¹, both of whom subsequently fitted third-order Birch and Modified Universal EoSs, respectively, to their data. Anomalies in the EoS data for the individual phases of Sm can be most readily visualised by using a simple “linearization” procedure whereby anomalies arising from changes in electronic structure can be distinguished from the “normal” compressive behaviour of regular metals³¹.

Figure 8 shows the APL linearized compression data for Sm in the form of a $\eta_{APL} - x$ plot

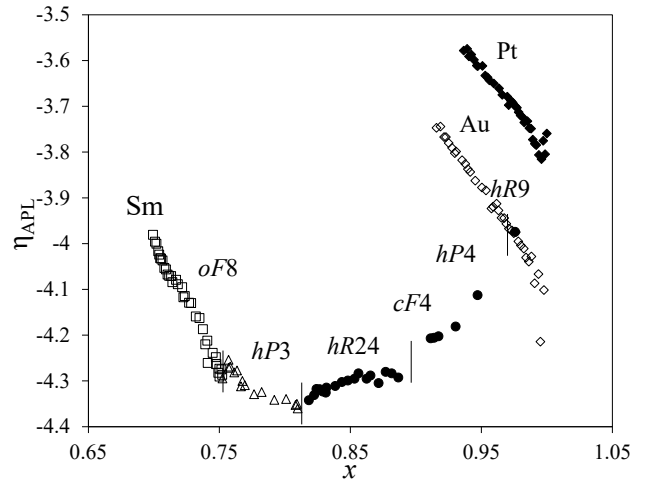


FIG. 8: Linearization of the compression of Sm shown in the form of an $\eta_{APL}-x$ plot. The data from the different phases of Sm are plotted using different symbols, and the “regular” compressibilities of Au and Pt, as calculated from the compression data of Dewaele *et al.*³², are shown for comparison.

$$\eta_{APL}(x) = \ln(px^5/p_{FG}) - \ln(1-x) \quad (2)$$

where $x = (V/V_0)^{1/3}$, $p_{FG} = a_{FG}(Z/V_0)^{5/3}$ and $a_{FG} = 0.02337 \text{ GPa} \cdot \text{nm}^5$, along with similarly-linearized data for the “regular” metals Au and Pt³². In such a plot, materials undergoing “normal” compression will show linear or quasi-linear behaviour, with the correct theoretical limit of $\eta(0) = 0$ at $x = 0$. The behaviour of Au and Pt clearly exhibits this form. In marked contrast to the very linear behaviour of Au and Pt, the data for Sm exhibit significant curvature, as noted previously by Zhao *et al.* for Sm³⁰, and by Grosshans and Holzapfel³³ for the trivalent lanthanides in general, and there is a clear change in gradient after the $hR24$ to $hP3$ transition at 43 GPa ($x \sim 0.81$) such that above 65 GPa ($x \sim 0.78$) the data from the $hP3$ and $oF8$ phases show “normal” linear behaviour, extrapolating to $\eta(0) \sim 0$. The $oF8$ phase of Sm might then be regarded as a “regular” metal.

Zhao *et al.* drew attention to these changes in gradient using their data collected over a smaller compression range, and using the incorrect structure for Sm above 90 GPa, and suggested that they arose from the change in the nature of the bonding in the different phases – from d -bonding in $hR24$, to intermediate $4f$ bonding in $hP3$ to itinerant $4f$ bonding in the $Fddd$ phase³⁰. The valence state of Yb metal has long been known to change on pressure increase^{34,35}, and Herbst and Wilkins³⁶ have predicted a valence transition in Sm from 3+ to 2+ at $\sim 100 \text{ GPa}$, close to the $hP3 \rightarrow oF8$ transition pressure of 92 GPa. Such a divalent state is reported to contribute to the high-temperature magnetic susceptibility of Sm at ambient pressure³⁷. Any valence change might be expected to have an effect the compressibility of Sm, but

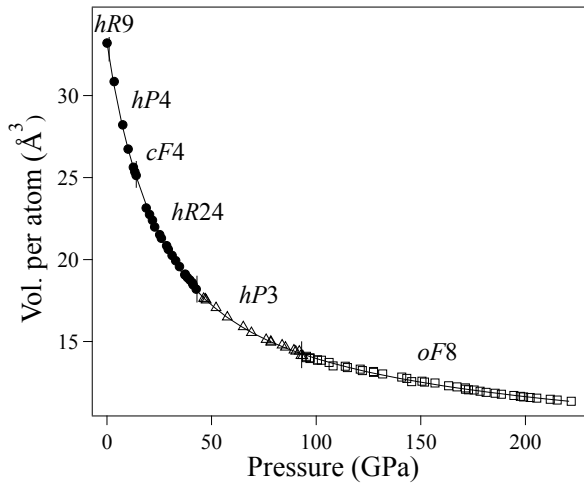


FIG. 9: The compressibility of Sm up to 222 GPa. The solid line shows the best fitting third-order AP3 EoS to the full compression curve.

as shown in Figure 8, there is no change in behavior at the $hP3 \rightarrow oF8$ transition. Recent L_3 XANES measurements on Tb to 65 GPa³⁸ and on Dy to 115 GPa³⁹ have explicitly ruled out the presence of a valence transition in either of these higher-Z lanthanide elements high pressure. Similar studies are required on Sm to see if it too remains trivalent to the highest pressures.

The data shown by Zhao *et al.* were from a variety of sources and exhibited considerable scatter, and, as said, used an incorrect structure for the $Fddd$ phase. Our data, collected from three samples of the same ingot, and the pressures for which were obtained using the same Cu EoS, show greater consistency and the changes in gradient in the linearized plot are therefore clearer. Our data to 222 GPa suggest that the discontinuity in incompressibility occurs between 45 and 65 GPa within the $hP3$ phase, with no further change being observed at the $hP3 \rightarrow oF8$ transition at 93 GPa.

As mentioned previously, both Zhao³⁰ and Chesnut¹¹ found that 3rd-order EoSs provided a better fit to their data, and Figure 9 shows the fit²⁹ of a 3rd-order APL (AP3) EoS to the full Sm compression curve with $K_0=40.6(11)$ GPa, $K'=1.58(6)$ and $K''=-0.0524(3)$. While the AP3 form fits the full compression curve much better than the AP2 form, the K_0 value 40.6 GPa is larger than the value of 31.6 GPa obtained by fitting only the data up to 43 GPa, and the value of 33 GPa reported previously³³. Close analysis of the AP3 fit reveals that it slightly underestimates the compressibility of the lower-pressure ($hR9$, $hP4$, $cF4$ and $hR24$) phases to 43 GPa (and therefore overestimates K_0) in order to better fit the higher pressure ($hP3$ and $oF8$) phases over the larger pressure range of 43 to 222 GPa.

For many “regular” solids, such as the $oF8$ phase of Sm above 93 GPa, c_2 , and all the higher order terms c_k

($k > 2$) of the APL EoS (see equation (1)) are zero⁴⁰, which implies for the corresponding AP1 form that

$$K'_{AP1} = 3 + (2/3) \cdot c_0 \quad (3)$$

The AP1 form thus has only two variables (V_0 and K_0) and it has been used to fit compression data from high-pressure phases when the pressure values for the first data points from that phase are small relative to the total pressure range for that phase⁴⁰. Despite having no data below 93 GPa, the 100+ GPa pressure range over which we have compression data for the $oF8$ phase meant that fitting the AP1 EoS to the $oF8$ phase was straightforward, giving values of $V_0=37.9(7)$ Å³/atom, $K_0=4.0(4)$ GPa, and $K'=7.07(6)$. Since the $oF8$ phase is unstable at low pressures, there is no experimental value of V_0 with which to compare the fitted value. However, the *calculated* value for this phase at ambient pressure and 0 K, as obtained from electronic structure calculations, is 35.95 Å³/atom⁴¹. Fixing V_0 at this calculated value, the AP1 fit gave $V_0=35.95$ Å³/atom (fixed), $K_0=5.08(1)$ GPa, and $K'=6.96(2)$, values not too dissimilar from those obtained from the free fit. While the small value of K_0 is that of an alkali metal, such as potassium ($K_0=3.1$ GPa) or sodium ($K_0=6.3$ GPa), the large value of K' results in a bulk modulus of ~ 390 GPa for the $oF8$ phase at 95 GPa.

Low-temperature magnetic studies of Sm to 50 GPa have shown that the magnetic transition temperatures closely follow the crystallographic symmetry during the $hR9 \rightarrow hP4 \rightarrow cF4 \rightarrow hR24$ transition sequence at high-pressures and low-temperatures⁴². More recently, Deng and Schilling have measured the magnetic ordering temperature T_0 of Sm metal up to 150 GPa and observed a strong increase in T_0 with pressure above 85 GPa from ~ 60 K to ~ 140 K⁹. This pressure is close to that of the $hP3 \rightarrow oF8$ transition in Sm at 300 K, and so it is likely that it is the $oF8$ phase of Sm that has a highly-correlated electron state, such as a Kondo lattice⁹. Given the very similar structural behaviour of Nd and Sm reported here, it is perhaps then surprising that the magnetic ordering temperature T_0 of Nd *decreases* sharply from 180 K to 120 K between 70 GPa and 110 GPa, where it has the $oF8$ structure at 300 K, before decreasing toward 0 K near 150 GPa⁶. Electronic structure calculations are needed both to cast light on the different magnetic behaviours seen in Sm and Nd, and to determine why the $oF16$ structure of Tb *et al.* is not seen in either Sm or Nd.

IV. CONCLUSIONS

The structure of Sm metal above 93 GPa is found to be face-centred orthorhombic ($oF8$), iso-structural with that observed in Nd, Am, Cm and Cf at high pressures, and iso-symmetric with the $oF16$ structure observed in Tb, Gd, Dy, Ho, Er and (probably) Tm¹⁸. High precision measurements of the compressibility of Sm reveal that it

becomes less compressible after the transition to the $hP3$ phase at 43 GPa, and that above 65 GPa its compressibility is that of a “regular” metal such as Au or Pt. Previous studies of Sm have linked changes in its crystal structure and compressibility to changes in its electronic structure, particularly changes from d -bonding in the $hR24$ structure, to intermediate $4f$ -bonding in the $hP3$ structure to itinerant $4f$ -bonding in the $oF8$ structure. Previous calculations which have suggested a delocalisation of the $4f$ shell in the 100 GPa pressure range were performed on the assumption that the post- $hP3$ phases of Sm has a body-centred tetragonal structure ($tI2$) rather than the $oF8$ structure reported here⁴³. Further calculations using the correct crystal structure are therefore now required.

V. ACKNOWLEDGMENTS

British Crown Owned Copyright 2020/AWE. Published with permission of the Controller of Her Britan-

nic Majesty’s Stationery Office. This work was supported by Grants (Grant No. EP/R02927X/1 and No. EP/R02992X/1) from the U.K. Engineering and Physical Sciences Research Council (EPSRC) and experimental facilities made available by DESY (Hamburg, Germany), a member of the Helmholtz Association HGF, and by Diamond Light Source (DLS). We would like to thank R.J. Husband for her assistance on beamline P02.2 at PETRA-III, and D. Daisenberger for his support on the I15 beamline at DLS. S.E. Finnegan and C.V. Storm are grateful to AWE for the award of CASE studentships. We would like to thank R.J. Angel for revising his EoSFit code in order to be able to fit both the AP2 and AP3 equations of state to our compression data. Finally, the preparation of this manuscript has benefited greatly from many discussions with W.B. Holzapfel about the APL equations of state.

* Electronic address: m.i.mcmahon@ed.ac.uk

- ¹ J. C. Duthie and D. G. Pettifor, Phys. Rev. Lett. **38**, 564 (1977), URL <https://link.aps.org/doi/10.1103/PhysRevLett.38.564>.
- ² B. Johansson and A. Rosengren, Physical Review B **11**, 2836 (1975).
- ³ D. A. Young, *Phase Diagrams of the Elements* (Univ of California Press, 1991).
- ⁴ H. Olijnyk and A. P. Jephcoat, Europhysics Letters (EPL) **69**, 385 (2005), ISSN 1286-4854, URL <http://dx.doi.org/10.1209/epl/i2004-10354-7>.
- ⁵ B. Johansson and A. Rosengren, Physical Review B **11**, 1367 (1975).
- ⁶ J. Song, W. Bi, D. Haskel, and J. S. Schilling, Physical Review B **95**, 205138 (2017).
- ⁷ J. Lim, G. Fabbris, D. Haskel, and J. S. Schilling, Physical Review B **91**, 174428 (2015).
- ⁸ J. Lim, G. Fabbris, D. Haskel, and J. Schilling, Physical Review B **91**, 045116 (2015).
- ⁹ Y. Deng and J. S. Schilling, Physical Review B **99**, 085137 (2019).
- ¹⁰ R. J. Husband, Ph.D. thesis, The University of Edinburgh (2015).
- ¹¹ G. N. Chesnut, Ph.D. thesis, The University of Alabama at Birmingham (2002).
- ¹² W. H. Zachariasen, Proceedings of the National Academy of Sciences **75**, 1066 (1978).
- ¹³ D. Errandonea, R. Boehler, B. Schwager, and M. Mezouar, Physical Review B **75**, 014103 (2007).
- ¹⁴ N. C. Cunningham, W. Qiu, K. M. Hope, H.-P. Liermann, and Y. K. Vohra, Physical Review B **76**, 212101 (2007).
- ¹⁵ G. K. Samudrala, S. A. Thomas, J. M. Montgomery, and Y. K. Vohra, Journal of Physics: Condensed Matter **23**, 315701 (2011).
- ¹⁶ J. M. Montgomery, G. K. Samudrala, G. M. Tsoi, and Y. K. Vohra, Journal of Physics: Condensed Matter **23**, 155701 (2011).
- ¹⁷ G. K. Samudrala and Y. K. Vohra, in *Handbook on the physics and chemistry of rare earths* (Elsevier, 2013), vol. 43, pp. 275–319.
- ¹⁸ M. I. McMahon, S. Finnegan, R. J. Husband, K. A. Munro, E. Plekhanov, N. Bonini, C. Weber, M. Hanfland, U. Schwarz, and S. G. Macleod, Physical Review B **100**, 024107 (2019).
- ¹⁹ S. Heathman, R. G. Haire, T. Le Bihan, A. Lindbaum, K. Litfin, Y. Méresse, and H. Libotte, Physical Review Letters **85**, 2961 (2000).
- ²⁰ S. Heathman, R. G. Haire, T. Le Bihan, A. Lindbaum, M. Idiri, P. Normile, S. Li, R. Ahuja, B. Johansson, and G. H. Lander, Science **309**, 110 (2005).
- ²¹ S. Heathman, T. Le Bihan, S. Yagoubi, B. Johansson, and R. Ahuja, Physical Review B **87**, 214111 (2013).
- ²² J. Akella, S. T. Weir, Y. K. Vohra, H. Prokop, S. A. Catledge, and G. N. Chesnut, Journal of Physics: Condensed Matter **11**, 6515 (1999).
- ²³ B. Johansson and A. Rosengren, Computers & Geosciences **94**, 162 (2016).
- ²⁴ A. P. Hammersley et al., European Synchrotron Radiation Facility Internal Report ESRF97HA02T **68**, 58 (1997).
- ²⁵ C. Prescher and V. B. Prakapenka, High Pressure Research **35**, 223 (2015).
- ²⁶ A. Snigirev, V. Kohn, I. Snigireva, and B. Lengeler, Nature **384**, 49 (1996), ISSN 1476-4687, URL <https://doi.org/10.1038/384049a0>.
- ²⁷ R. J. Husband, I. Loa, K. Munro, and M. I. McMahon, Journal of Physics: Conference Series **500**, 032009 (2014), URL <https://doi.org/10.1088%2F1742-6596%2F500%2F3%2F032009>.
- ²⁸ W. B. Holzapfel, International Journal of High Pressure Research **16**, 81 (1998).
- ²⁹ R. J. Angel, M. Alvaro, and J. Gonzalez-Platas, Zeitschrift für Kristallographie-Crystalline Materials **229**, 405 (2014).
- ³⁰ Y. C. Zhao, F. Porsch, and W. B. Holzapfel, Physical Review B **50**, 6603 (1994).

- ³¹ W. B. Holzapfel, in *Correlations in Condensed Matter under Extreme Conditions* (Springer, 2017), pp. 91–106.
- ³² A. Dewaele, P. Loubeyre, and M. Mezouar, *Physical Review B* **70**, 094112 (2004).
- ³³ W. A. Grosshans and W. B. Holzapfel, *Physical Review B* **45**, 5171 (1992).
- ³⁴ K. Syassen, G. Wortmann, J. Feldhaus, K. H. Frank, and G. Kaindl, *Phys. Rev. B* **26**, 4745 (1982), URL <https://link.aps.org/doi/10.1103/PhysRevB.26.4745>.
- ³⁵ A. Fuse, G. Nakamoto, M. Kurisu, N. Ishimatsu, and H. Tanida, *Journal of Alloys and Compounds* **376**, 34 (2004), ISSN 0925-8388, URL <http://www.sciencedirect.com/science/article/pii/S0925838804000593>.
- ³⁶ J. F. Herbst and J. W. Wilkins, *Phys. Rev. B* **29**, 5992 (1984), URL <https://link.aps.org/doi/10.1103/PhysRevB.29.5992>.
- ³⁷ N. S. Uporova, S. A. Uporov, and V. E. Sidorov, *Journal of Experimental and Theoretical Physics* **114**, 281 (2012), ISSN 1090-6509, URL <https://doi.org/10.1134/S1063776112010086>.
- ³⁸ G. Fabbri, T. Matsuoka, J. Lim, J. R. L. Mardegan, K. Shimizu, D. Haskel, and J. S. Schilling, *Phys. Rev. B* **88**, 245103 (2013), URL <https://link.aps.org/doi/10.1103/PhysRevB.88.245103>.
- ³⁹ J. S. Schilling, in *Correlations in Condensed Matter under Extreme Conditions: A tribute to Renato Pucci on the occasion of his 70th birthday*, edited by G. G. N. Angilella and A. La Magna (Springer International Publishing, Cham, 2017), pp. 47–56, URL https://doi.org/10.1007/978-3-319-53664-4_4.
- ⁴⁰ W. B. Holzapfel, *The Review of High Pressure Science and Technology* **11**, 55 (2001).
- ⁴¹ E. Plekhanov, N. Bonini, and C. Weber, unpublished.
- ⁴² C. R. Johnson, G. M. Tsoi, and Y. K. Vohra, *Journal of Physics: Condensed Matter* **29** (2016).
- ⁴³ P. Söderlind, O. Eriksson, J. M. Wills, and A. M. Boring, *Physical Review B* **48**, 5844 (1993).